

# NUMERICAL STUDY OF THE SERRE-GREEN-NAGHDI EQUATIONS IN 2D

SERGEY GAVRILYUK AND CHRISTIAN KLEIN

**ABSTRACT.** A detailed numerical study of solutions to the Serre-Green-Naghdi (SGN) equations in 2D with vanishing curl of the velocity field is presented. The transverse stability of line solitary waves, 1D solitary waves being exact solutions of the 2D equations independent of the second variable, is established numerically. The study of localized initial data as well as crossing 1D solitary waves does not give an indication of existence of stable structures in SGN solutions localized in two spatial dimensions. For the numerical experiments, an approach based on a Fourier spectral method with a Krylov subspace technique is applied.

## 1. INTRODUCTION

We present a numerical study of solutions to the Serre–Green–Naghdi (SGN) equations. The SGN equations are classical dispersive shallow water equations which can be derived from the free surface Euler equations both by depth averaging [22, 23, 7, 8] and via Hamilton’s principle of stationary action [19, 21]. In dimensional form, the SGN equations for a flat bottom are:

$$(1a) \quad h_t + \nabla \cdot (h\bar{\mathbf{u}}) = 0,$$

$$(1b) \quad (h\bar{\mathbf{u}})_t + \nabla \cdot (h\bar{\mathbf{u}} \otimes \bar{\mathbf{u}} + p\mathbf{I}) = 0, \quad p = \frac{gh^2}{2} + \frac{h^2}{3}\ddot{h}.$$

Here  $h$  is the water depth,  $\bar{\mathbf{u}} = (u_x, u_y)^T$  is the depth averaged velocity,  $\mathbf{x} = (x, y)^T$  are the classical Cartesian coordinates,  $g$  is the gravity acceleration,  $\nabla \cdot$  is the divergence operator,  $\dot{h} = \frac{\partial h}{\partial t} + \bar{\mathbf{u}} \cdot \nabla h$  is the material derivative along the depth averaged velocity, two “dots” denote the corresponding second material derivative. As a consequence, they admit the energy conservation law in the form:

$$(2) \quad (hE)_t + \nabla \cdot (hE\bar{\mathbf{u}} + p\bar{\mathbf{u}}) = 0, \quad E = \frac{|\bar{\mathbf{u}}|^2}{2} + \frac{gh}{2} + \frac{\dot{h}^2}{6}.$$

A class of generalized potential flows which are exact solutions to the 2D SGN equations was introduced in [5]. In particular, this class of flows is well defined

---

*Date:* March 4, 2024.

CK thanks for support by the EIPHI Graduate School (contract ANR-17-EURE-0002) and by the European Union Horizon 2020 research and innovation program under the Marie Skłodowska-Curie RISE 2017 grant agreement no. 778010 IPaDEGAN. .

if the non-cavitation condition ( $h > 0$ ) is fulfilled. It is assumed throughout the manuscript. To study such 2D solutions numerically, we apply an extension of the numerical approach [1] for the 1D SGN equation to two spatial dimensions. The method is again based on a Fourier spectral method in the spatial variables with the Krylov subspace technique GMRES [20] to invert an elliptic equation for an auxiliary quantity (the appearance of the quantity  $\ddot{h}$  in (1b) implies that at least one elliptic equation has to be solved in each time step as will be detailed below). The time integration will be done with the standard explicit 4th order Runge-Kutta method.

This code will be applied to interesting initial data in the context of the SGN equations. First we address the transverse stability of the line solitary waves: the explicitly known solitary wave solution for the 1D SGN equations (13) can be seen as a  $y$ -independent exact solution to the 2D SGN equations, i.e., an infinitely extended travelling wave called *line solitary wave*. We study various perturbations of this line solitary wave numerically for a range of velocities relevant in applications. In this sense we study what is known as the transverse stability of such infinitely extended structures. The numerical results give strong evidence to the following

**Main conjecture I:**

*The line solitary wave (13) is transversely stable as a solution to the 2D SGN equations.*

The stability of the line solitary wave is an indication that the behavior of solutions to the SGN equations is similar to the one of solutions to the Kadomtsev-Petviashvili (KP) II equations, see [10] for a recent comprehensive review with many references. For the KP II equation, the Korteweg-de Vries (KdV) soliton gives a line soliton solution which is stable for KP II, but not for the so-called KP I equation. In the latter case the line soliton is unstable against the formation of so-called lump solitons, travelling waves localised in two dimensions. The KP II equation does not have travelling wave solutions localised in two dimensions, and it has a *defocusing* effect on localised initial data: there are no stable structures in their solutions localised in 2D, hump-like initial data are simply radiated away to infinity. By studying localised initial data for SGN, we give strong evidence for the fact that SGN has a defocusing effect as KP II, and that there are no stable solitary waves localised in two dimensions. We get the following

**Main conjecture II:**

*There are no stable SGN solitary waves localised in two dimensions. The equation has a defocusing effect.*

The paper is organised as follows: in section 2 we collect some basic facts of the 2D SGN equations. In section 3 we briefly describe the applied numerical approach. The transverse stability of the line solitary waves is studied in section 4. In section 5 we consider the time evolution of the formal superposition of two line solitary waves, one in  $x$ , the other in  $y$ . Again no stable structures are observed in the time evolution of these data. In section 6 we study the time evolution of

hump-like initial data. It is shown that Gaussian initial data evolve into an annular structure with a central depression. We add some concluding remarks in section 7.

## 2. BASIC FACTS

In this section, we collect some basic facts on the SGN equation and give a form of the equations suitable for the planned numerical treatment.

**2.1. Introduction of the potential  $\varphi$ .** One can introduce the variable  $\mathbf{v} = (v_x, v_y)^T$  defined as [19, 21, 5]:

$$(3) \quad \mathbf{v} = \bar{\mathbf{u}} - \frac{1}{3h} \nabla (h^3 \nabla \cdot \bar{\mathbf{u}}) = \bar{\mathbf{u}} + \frac{1}{h} \nabla \left( \frac{h^2 \dot{h}}{3} \right)$$

and the potential  $\varphi$  such that  $\mathbf{v} = \nabla \varphi$ . The variable  $\mathbf{v}$  is the tangent velocity of the fluid at the free surface [4], and  $\varphi$  is the generalized flow potential. One can prove that if, initially,  $\text{curl } \mathbf{v} = 0$ , it will stay zero for any time [5]. In the following, we consider this special class of generalized potential flows. The notion of generalized potential flows has a sense only in the 2D case because all one-dimensional flows are obviously irrotational. In the one-dimensional case the SGN equations admit, in particular, one-dimensional solitary wave solutions [23]. The linear stability of solitary waves of small amplitude has been analytically proven in [17], see for instance [1] for a numerical investigation. Here, we study their stability with respect to multi-dimensional perturbations in the class of generalized potential flows introduced above.

**2.2. Governing equations of potential flows of the SGN equations.** Introducing the variable  $\sigma$

$$(4) \quad \sigma = \frac{h^2}{3} \dot{h},$$

and as above the potential  $\varphi$ ,

$$(5) \quad \nabla \varphi = \bar{\mathbf{u}} + \frac{1}{h} \nabla \sigma,$$

one can rewrite the momentum equation (1b) in the form of the generalized Bernoulli equation [5]:

$$(6) \quad \varphi_t + \nabla \varphi \cdot \bar{\mathbf{u}} + gh - \frac{1}{2} \dot{h}^2 - \frac{1}{2} |\bar{\mathbf{u}}|^2 = gh_\infty, \quad \bar{\mathbf{u}} = \nabla \varphi - \frac{1}{h} \nabla \sigma.$$

Here  $h_\infty = \text{const}$  is the fluid depth at infinity, the corresponding averaged velocity is vanishing at infinity. An equivalent form is

$$(7) \quad \varphi_t + \frac{|\nabla \varphi|^2}{2} - \frac{|\nabla \sigma|^2}{2h^2} + gh - \frac{9\sigma^2}{2h^4} = gh_\infty.$$

Complemented by the mass conservation law, the system reads:

$$(8a) \quad h_t + \nabla \cdot (h \nabla \varphi) = \Delta \sigma,$$

$$(8b) \quad \varphi_t + \frac{|\nabla \varphi|^2}{2} - \frac{|\nabla \sigma|^2}{2h^2} + gh - \frac{9\sigma^2}{2h^4} = gh_\infty,$$

$$(8c) \quad \frac{3\sigma}{h^3} - \nabla \cdot \left( \frac{\nabla \sigma}{h} \right) = -\Delta \varphi.$$

The equation (8c) can be formally rewritten in the form

$$(9) \quad \mathcal{L}[\sigma] = -\Delta \varphi, \quad \text{with} \quad \mathcal{L}[\sigma] = \frac{3\sigma}{h^3} - \nabla \cdot \left( \frac{\nabla \sigma}{h} \right).$$

Then

$$(10) \quad \sigma = -\mathcal{L}^{-1}[\Delta \varphi].$$

The boundary conditions as  $|\mathbf{x}| \rightarrow \infty$  are:

$$(11) \quad \nabla \varphi \rightarrow 0, \quad \sigma \rightarrow 0, \quad h \rightarrow h_\infty > 0.$$

These boundary conditions are adapted for the study of the solitary waves.

**2.3. Conserved quantities.** The total mass, total momentum and total energy are conserved. Their integral form for boundary conditions (11) is :

$$(12a) \quad \frac{d\mathcal{M}}{dt} = \frac{d}{dt} \iint_{-\infty}^{+\infty} (h - h_\infty) dx dy = 0,$$

$$(12b) \quad \frac{d\mathcal{P}}{dt} = \frac{d}{dt} \iint_{-\infty}^{+\infty} h \bar{\mathbf{u}} dx dy = 0,$$

$$(12c) \quad \frac{d\mathcal{E}}{dt} = \frac{d}{dt} \iint_{-\infty}^{+\infty} \left( \frac{h|\bar{\mathbf{u}}|^2}{2} + \frac{3\sigma^2}{2h^3} + \frac{g(h - h_\infty)^2}{2} \right) dx dy = 0.$$

Compared to (2), we used the total mass conservation (12a) to transform the local energy density in (2) to the form (12c).

**2.4. 1D solitary waves.** Let  $x$  be the one-dimensional space coordinate, and  $u$  be the velocity in  $x$ -direction. Let  $\xi = x - ct$  be the travelling coordinate, with  $c > 0$  being the wave velocity, and  $\bar{\mathbf{u}} = (u_c, 0)^T$ . In the following, ‘‘prime’’ means the derivative with respect to  $\xi$ . Then the solution (for  $c^2 > gh_\infty$ ) is [23]:

$$(13) \quad h_c = h_\infty + \frac{(c^2 - gh_\infty)}{g} \operatorname{sech}^2 \left( \frac{\xi}{2ch_\infty} \sqrt{3(c^2 - gh_\infty)} \right), \quad h_c(u_c - c) = m, \quad m = -ch_\infty,$$

and

$$(14) \quad \sigma = m(h_c^2)' / 6, \quad \varphi' = c + \frac{m}{h_c} \left( 1 + \frac{(h_c^2)''}{6} \right).$$

### 3. NUMERICAL APPROACH

In this section we summarize the numerical approach to be applied in this paper. As in [1], we will use a Fourier spectral method with the Krylov subspace technique GMRES [20].

The basic idea is to solve the SGN equations in Fourier space and to approximate the Fourier transform with a discrete Fourier transform (DFT) which is computed with a fast Fourier transform (FFT). We use the following convention for the Fourier transform for sufficiently regular and localized functions  $g$ :

$$\begin{aligned} \forall(k_x, k_y) \in \mathbb{R}^2, \quad \widehat{g}(k_x, k_y) &:= \int_{\mathbb{R}^2} e^{-i(k_x x + k_y y)} g(x, y) dx dy \\ \forall(x, y) \in \mathbb{R}^2, \quad g(x) &= \frac{1}{(2\pi)^2} \int_{\mathbb{R}^2} e^{i(k_x x + k_y y)} \widehat{g}(k_x, k_y) dk_x dk_y. \end{aligned}$$

It is well known that smooth rapidly decreasing or smooth periodic functions  $g(x, y)$  in each variable can be expanded in a Fourier series in both  $x$  and  $y$ , and that the coefficients of this series decrease rapidly in both indices. The DFT can be seen as a truncated Fourier series, and the numerical error in truncating is of the magnitude of the first neglected coefficients, see for instance [25] and references therein. In an abuse of notation, we will in the following denote the DFT of a function  $g(x, y)$  ( $x$  and  $y$  being some vectors of collocation points) also by  $\widehat{g}$ . Derivatives are approximated in standard way, e.g.,  $\widehat{g}_x \approx ik_x \widehat{g}$ .

This approach is numerically efficient and of high accuracy for functions vanishing rapidly at infinity or being periodic. Therefore we will establish equations for  $\mathbf{v} = \nabla\varphi$  having in contrast to  $\varphi$  the property to vanish at infinity. For this, we replaced  $\nabla\varphi$  by  $\mathbf{v}$  excepting (8b) written in the form

$$(15) \quad \mathbf{v}_t + \nabla \cdot \left( \frac{|\mathbf{v}|^2}{2} - \frac{|\nabla\sigma|^2}{2h^2} + gh - \frac{9\sigma^2}{2h^4} \right) = 0.$$

If, initially,  $\text{curl}\mathbf{v} = 0$ , it will be vanishing for any  $t > 0$ . Since derivatives in a Fourier spectral method are computed by multiplications with the dual variable in Fourier space, this is also the case for the numerical approach. On the other hand we are interested in minimizing the number of elliptic PDEs to be solved. If we used (1b) for  $h\bar{\mathbf{u}}$  (note that the flux in (1b) depends of  $\dot{h}$ ), two such elliptic PDEs would need to be solved for each time step instead of one for  $\sigma$ . Last not least we want to avoid the computation of high order derivatives as much as possible since this will lead to rounding errors that can pile up during the time evolution.

For these reasons we work with the variables  $h$  and  $\mathbf{v}$  in the following and compute  $\sigma$  in each time step via

$$(16) \quad \frac{3\sigma}{h^3} - \nabla \cdot \left( \frac{\nabla\sigma}{h} \right) = -\nabla \cdot \mathbf{v}.$$

This is done as in [1] in Fourier space with the Krylov subspace technique GMRES [20]. Concretely we discretize in  $x$  and  $y$  in standard fashion for the DFT in each variable which means we introduce the collocation points  $x_n = -L_x\pi + n2\pi L_x$ ,  $n = 1, \dots, N_x$  and  $y_m = -L_y\pi + m2\pi L_y$ ,  $m = 1, \dots, N_y$ . Thus we work on  $\mathbb{T}^2$  with periods  $2\pi L_x$  in  $x$ -direction and  $2\pi L_y$  in  $y$ -direction. The positive numbers  $L_x, L_y$  are chosen such that they correspond to the actual period in the respective direction in the case of a periodic solution or, for rapidly decreasing functions, that the function and its relevant derivatives vanish within the finite numerical precision. After this discretisation, the quantities  $h, v_x$  and  $v_y$  become  $N_x \times N_y$  matrices. Equation (16) takes the form  $\mathcal{L}\sigma = b$  where  $b$  is a vector built from the matrix  $\nabla \cdot \mathbf{v}$  after discretisation in a natural way by just writing the columns of the matrix in the form of a long vector. In the same way  $\mathcal{L}$  is a  $N_x N_y \times N_x N_y$  matrix the inverse of which is computed approximately via GMRES. Note that it is important to use a preconditioner  $\mathcal{M}$  such that GMRES computes the solution of  $\mathcal{M}^{-1}\mathcal{L}\sigma = \mathcal{M}^{-1}b$ . We choose as a preconditioner  $\mathcal{L}$  for  $h = 1$ , the asymptotic value, i.e.,  $\mathcal{M} = 3 + k_x^2 + k_y^2$ .

For the time integration of the SGN equations we apply as in [1] the standard explicit Runge-Kutta method of fourth order. This can be done directly for the first equation of (1). The equation (8b) is written as  $\varphi_t = F$  and then differentiated with respect to  $x$  and  $y$  by multiplying with  $k_x$  and  $k_y$  in Fourier space. This yields equations for  $\mathbf{v}_t$  which are again integrated with the fourth order Runge-Kutta method. Note that GMRES is started with the last computed value for  $\sigma$  as an initial guess. For small time steps,  $\sigma$  does not change much over one time step, and consequently GMRES converges rapidly.

Note, however, that this is only the case as long as there is enough resolution in space as indicated by the decrease of the DFT coefficients. If they no longer decrease to machine precision during time evolution, GMRES will converge more slowly or not to the wanted accuracy, and rounding errors will pile up. To avoid such scenarios, we use a *Krasny filter* [12], i.e., we put all DFT coefficients with modulus smaller than  $10^{-12}$  equal to zero. However, it is recommended to provide enough resolution in space during the whole computation since GMRES will become slower in underresolved cases. Even if there is enough resolution, GMRES will take around 90 % of the computation time.

The accuracy of the time integration is controlled via the conservation of the numerically computed energy. Due to unavoidable numerical errors, the computed energy will depend on time, and the relative conservation of the energy can be used as discussed for instance in [9] to estimate the resolution in time: typically this quantity overestimates the numerical accuracy by 2 orders of magnitude. In all experiments reported below, relative energy conservation is better than  $10^{-5}$  and thus above plotting accuracy. Since no explicit full 2D solution to the SGN equations in the class of functions studied here is known, we can only test the 1D solutions. If we propagate the exact 1D soliton with  $N_x = 2^{10}$  and  $N_y = 2^7$  Fourier

modes with  $L_x = 10$  and  $L_y = 2$  and  $N_t = 10^3$  time steps for  $t \leq 1$ , we get energy conservation to the order of  $10^{-14}$  as can be seen on the left of Fig. 1, essentially the optimum that can be achieved with double precision. On the right of the same figure, we show the difference between numerical and exact solution for  $h$  as a function of time. It can be seen that numerical errors in the time integration pile up as usual and increase with time, but that the solitary wave can be propagated with machine precision.

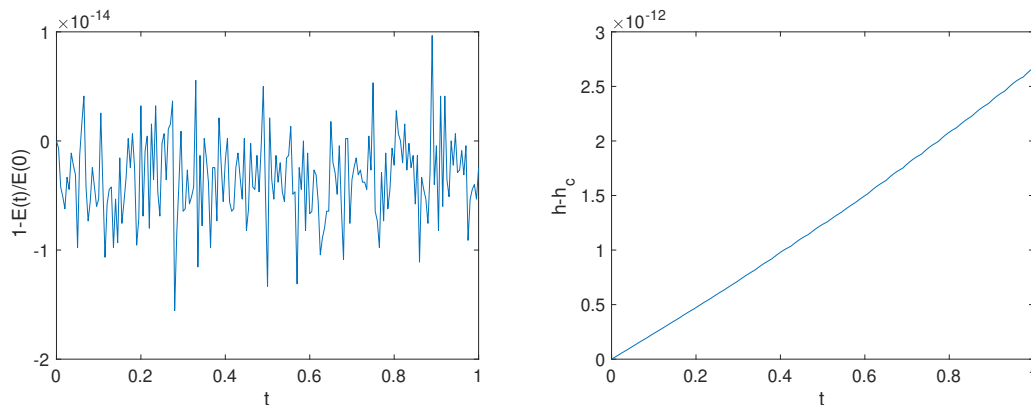


FIGURE 1. Propagation of the line soliton with  $c = 1.7$ . We show on the left the relative conservation of the numerically computed energy, and on the right the difference between exact and numerical solution for  $h$ .

#### 4. TRANSVERSE STABILITY OF LINE SOLITARY WAVES

The 1D solitary wave (13) can be seen as a  $y$ -independent solution to the 2D SGN equations, i.e., a traveling wave solution infinitely extended in  $y$ -direction. If the solution (13) is considered in dependence of  $y$  instead of  $x$ , it can be seen as an  $x$ -independent solution to the 2D SGN equations. We call such solutions *line solitary waves*. In this section we consider perturbations of such line solitary waves (for simplicity we consider an infinite extension in  $y$ ). Numerically, the situation is studied on  $\mathbb{T}^2$  with period  $2\pi L_x$  in  $x$ -direction and  $2\pi L_y$  in  $y$ -direction. We consider in this section the case  $c = 1.7$ . Cases with smaller and larger velocity have been studied as well, but the results are very similar to what is shown below and will thus not be presented. We will always put  $h_\infty = g = 1$  in the following. We always show  $\bar{\mathbf{u}}$  since it is more important in applications though the code is set up for  $\mathbf{v}$ .

In this section we study various perturbations of the line solitary waves and show that they are numerically stable giving strong evidence to the first part of the main conjecture.

**4.1. Deformed line solitary wave.** As a first perturbation we consider a deformed line solitary wave, i.e., initial data of the form

$$(17a) \quad h(x, y, 0) = 1 + (c^2 - 1) \operatorname{sech}^2 \left( \frac{x - x_0 - 0.1 \cos(y)}{2c} \sqrt{3(c^2 - 1)} \right),$$

$$(17b) \quad v_x(x, y, 0) = c - \frac{c}{h} \left( 1 + \frac{(h^2)_{xx}}{6} \right), \quad v_y(x, y, 0) = 0.$$

Here  $x_0 = -10$ . The resulting initial data for  $h$ ,  $u_x$  and  $u_y$  are shown as the first figure in Fig. 2, Fig. 3 and Fig. 4 respectively.

We use  $N_x = 2^{10}$  and  $N_y = 2^7$  Fourier modes with  $L_x = 10$  and  $L_y = 2$  and  $N_t = 10^3$  time steps for  $t \leq 10$ . The function  $h$  for these initial data is shown in Fig. 2 for several times. It can be seen that the initial deformation leads to a stronger one which eventually results in an emission of radiation from the deformed line solitary wave. The final state appears to be an unperturbed line solitary wave.

The behavior of the quantity  $u_x$  is very similar as can be seen in Fig. 3. The initial deformation leads to radiation plus the unperturbed  $u_x$  for the line soliton.

The quantity  $u_y$  on the other hand vanishes in the unperturbed case and only shows in Fig. 4 radiative behavior during time evolution (the amplitude is always considerably smaller than the ones of  $h$  in Fig. 2 and  $u_x$  in Fig. 3).

Note that the initial data (17) are a perturbation of the order of 10% and thus by no means small. However, it appears that the final state is the unperturbed line solitary wave which would indicate its stability. To make this more evident, we show in Fig. 5 the difference between the final state and the unperturbed solitary wave (13) centered at  $x_s = 6.995$ , the numerically determined location of the maximum of  $h$ . In Fig. 5 we consider the difference between  $h$  and the value  $h_c$  for the solitary wave (13) with  $c = 1.7$  as well as the respective difference between  $u_x$  and the unperturbed  $u_c$  (13). It can be seen that this difference is of the order of the quantity  $u_y$ , no trace of the line solitary wave can be seen in the difference. This provides strong numerical evidence for the conjecture that a perturbation of the line solitary wave leads to the unperturbed solitary wave plus radiation for sufficiently large times.

**4.2. Line solitary wave plus Gaussian perturbation.** We consider initial data with a localized perturbation of the form

$$(18a) \quad h(x, y, 0) = h_c(x - x_0) \pm 0.1 \exp(-(x - x_0)^2 - y^2),$$

$$(18b) \quad v_x(x, y, 0) = c - \frac{c}{h} \left( 1 + \frac{(h^2)_{xx}}{6} \right), \quad v_y(x, y, 0) = 0,$$



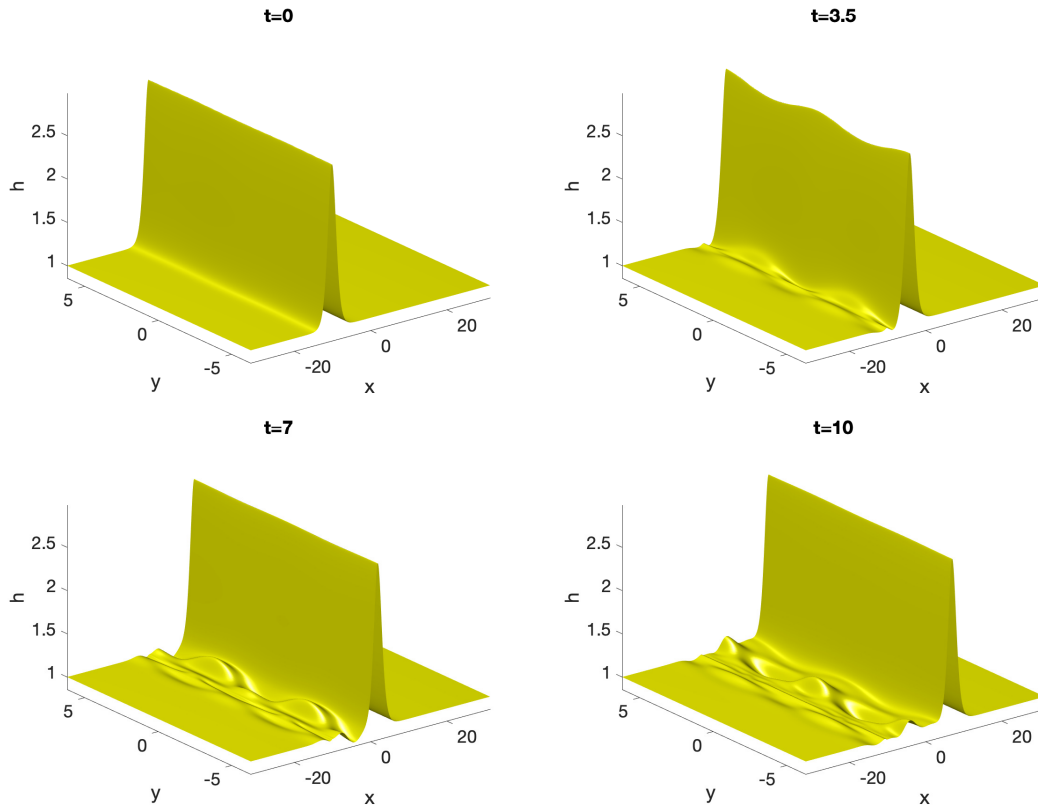


FIGURE 2. Solution  $h$  to the 2D SGN equation for initial data being a deformed line solitary wave of the form (17) for several values of time.

i.e., a solitary wave with a small Gaussian perturbation. We work with  $N_x = 2^{11}$ ,  $N_y = 2^8$ ,  $L_x = 20$ ,  $L_y = 2$ ,  $x_0 = -20$  and  $N_t = 2000$  time steps for  $t \leq 20$  (for larger times the same time step is used). The DFT coefficients decrease during the whole computation to the order of  $10^{-7}$ , relative energy conservation is of the order of  $10^{-9}$ .

The solution  $h$  for both initial data (18) at the final time can be seen in Fig. 6. It appears that the final state is once more the unperturbed line solitary wave plus radiation.

The corresponding velocities  $u_x$  at the final time are shown in Fig. 7. Again this can be interpreted as a line soliton plus radiation.

The velocities  $u_y$  also show the expected behavior, i.e., only radiation, as can be seen in Fig. 8. Its magnitude is considerably smaller than the initial perturbation which stresses the stability of the line solitary wave.

The  $L^\infty$  norms of the solution  $h$  can be seen in Fig. 9. They show the typical oscillations around a presumed final state (the small oscillations are due to the fact

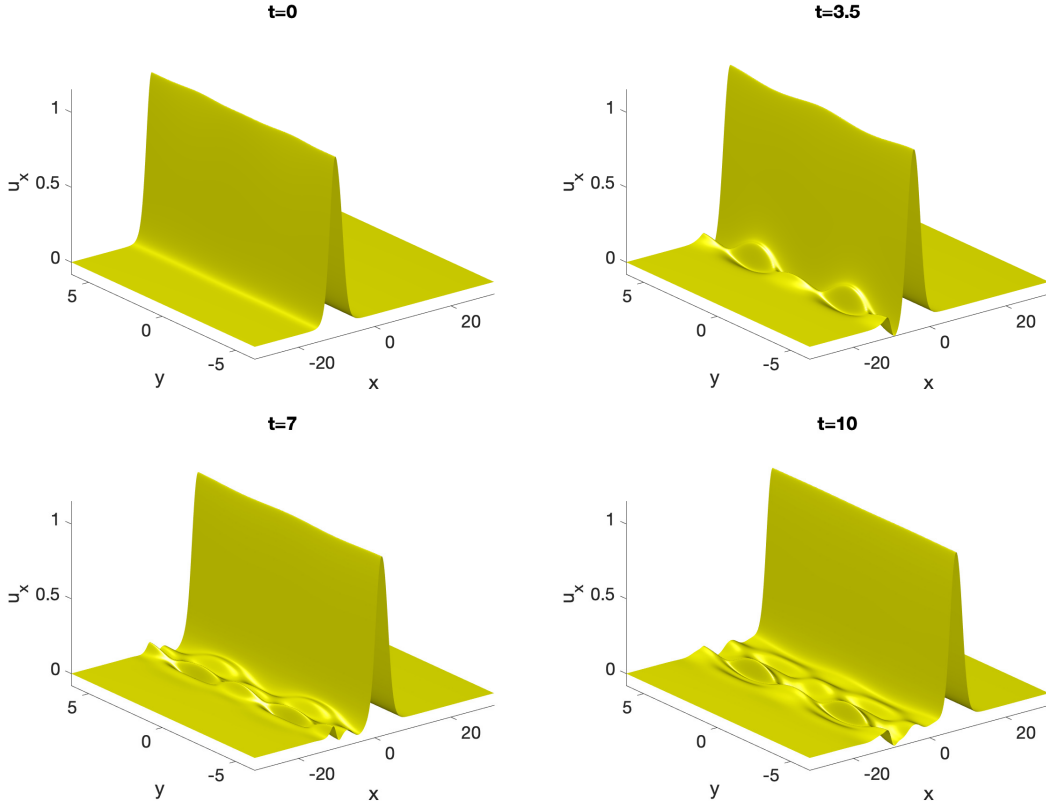


FIGURE 3. Solution  $u_x$  to the 2D SGN equation for initial data being a deformed line solitary wave of the form (17) for several values of time.

that we determine the  $L^\infty$  norm on grid points which not necessarily correspond to the location of the maximum). Since we consider a perturbation with a higher respectively lower mass of several percents, the  $L^\infty$  norm of this final state will have a slightly different value than the unperturbed soliton, and thus a slightly different velocity  $c$ . Note that there are stronger oscillations in the case with smaller mass. This indicates that one does not get as rapidly close to the final state as in the case with larger mass though the final time is the same, which is why we considered longer times in the case of a  $-$  sign in (18). The final time is also at least twice than what was taken for the initial data (17).

In order to check whether the final state is indeed a line solitary wave, we consider once more the difference between the 1D solution (13) and the above 2D solution for  $t = 20$ . The former is taken at the location of the maximum as before, the value of  $c$  is obtained by fitting this maximum to the maximum of expression (13). The resulting differences for  $h$  and  $u_x$  are shown in Fig. 10. It can be seen that the difference is of the order of magnitude of the radiation. As indicated by

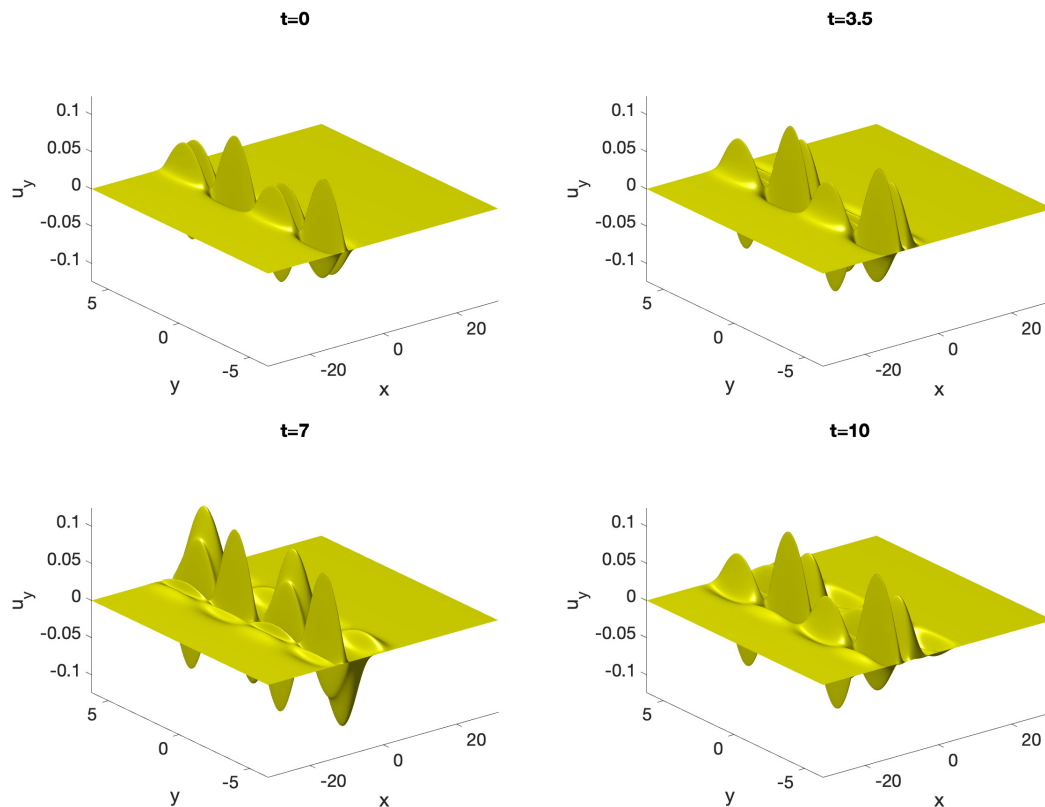


FIGURE 4. Solution  $u_y$  to the 2D SGN equation for initial data being a deformed line solitary wave of the form (17) for several values of time.

the  $L^\infty$  norm in Fig. 9, the final state will be reached in the  $-$  case in (18) only for even larger times.

## 5. INITIAL DATA OF CROSSING SOLITARY WAVES

Integrable equations in 2D as the KP II equation have multi-line-solitons as exact solutions, i.e. several line solitons crossing at certain angles forming time dependent patterns of solitons, see e.g. [11] and references therein. Since SGN does not appear to be completely integrable, no exact multi-solitary waves are expected. But we can discuss the time evolution of initial data which are simply the superposition of one line soliton in  $x$ -direction and one in  $y$ -direction. Concretely

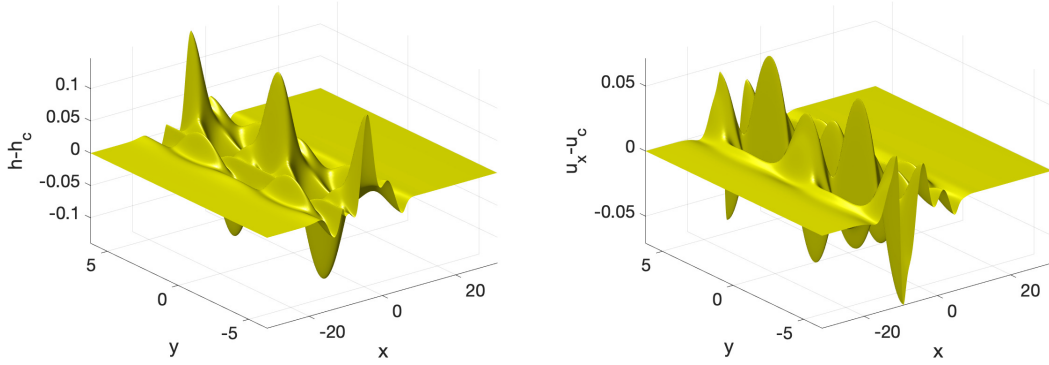


FIGURE 5. Difference between the solution to the 2D SGN equation for initial data being a deformed line solitary wave of the form (17) for  $t = 10$  and an unperturbed line solitary wave centered at  $x_s = 6.995$ : on the left for  $h$ , on the right for  $u_x$ .

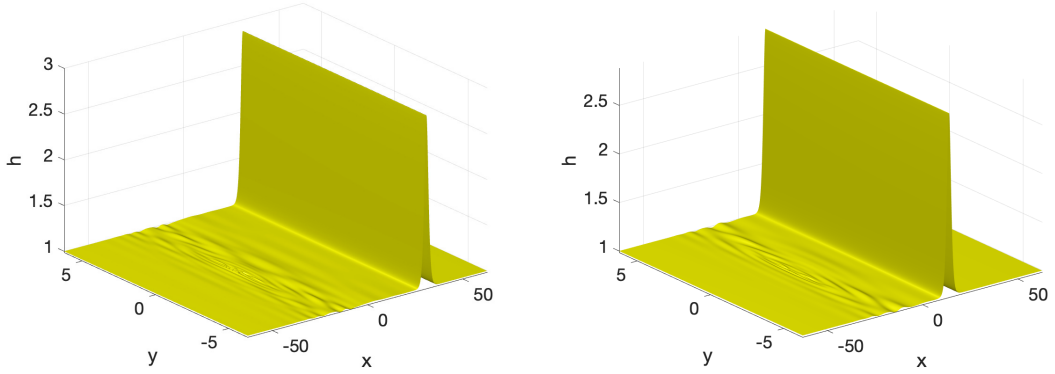


FIGURE 6. Solution  $h$  to the 2D SGN equation for initial data of the form (18): on the left for the minus sign in (18) for  $t = 30$ , on the right for the plus sign for  $t = 20$ .

we consider the following example,

$$(19a) \quad h(x, y, 0) = h_c(x) + h_c(y)$$

$$(19b) \quad v_x(x, y, 0) = c - \frac{c}{h_c(x)} \left( 1 + \frac{((h_c(x))^2)_{xx}}{6} \right),$$

$$(19c) \quad v_y(x, y, 0) = c - \frac{c}{h_c(y)} \left( 1 + \frac{((h_c(y))^2)_{yy}}{6} \right).$$

We consider the example  $c = 1.7$  for both line solitary waves which leads to a symmetric situation. We use  $N_x = N_y = 2^{10}$  Fourier modes with  $L_x = L_y = 10$

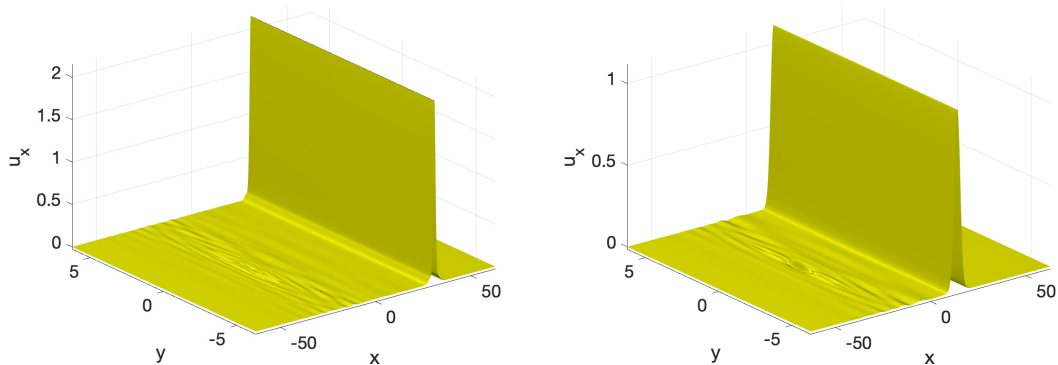


FIGURE 7. Solution  $u_x$  to the 2D SGN equation for initial data of the form (18): on the left for the  $-$  sign in (18) for  $t = 30$ , on the right for the  $+$  sign for  $t = 20$ .

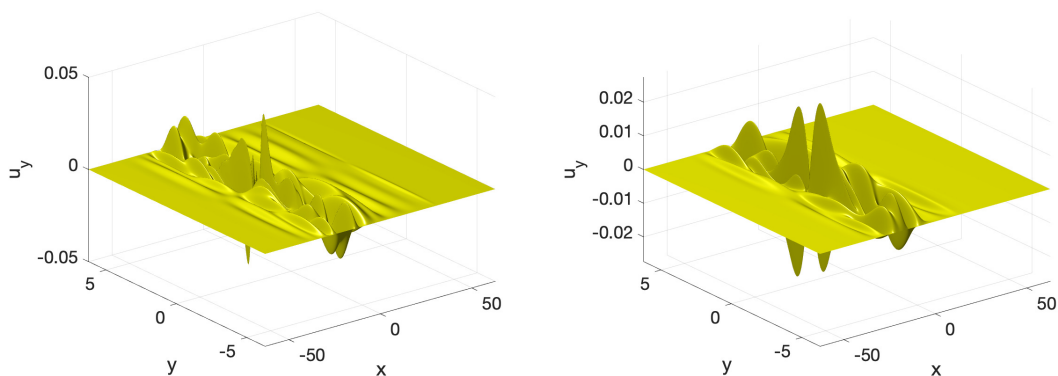


FIGURE 8. Solution  $u_y$  to the 2D SGN equation for initial data of the form (18): on the left for the  $-$  sign in (18) for  $t = 30$ , on the right for the  $+$  sign for  $t = 20$ .

and  $N_t = 10^3$  time steps for  $t \leq 10$ . The energy is conserved during the whole computation relatively to the order of  $10^{-9}$ .

The solution  $h$  for the initial data (19) is shown for several values of time in Fig. 11. Note that this is not a perturbation of one line solitary wave, but simply a formal sum of two such solutions. Since the SGN equation is nonlinear, no dynamics close to a single line solitary wave can be expected in such a case. It can be seen that the solitary waves decouple from the central hump. Even at longer times, we do not discover a stable structure localised in 2D.

The solution  $u_x$  is localized in  $y$ -direction as can be seen in Fig. 12. It appears to slowly decompose near the center where the second solitary wave is superposed.

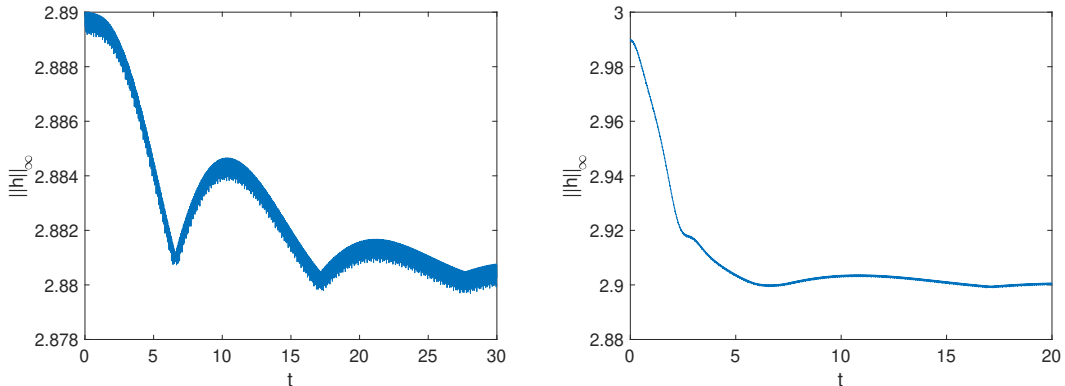


FIGURE 9.  $L^\infty$  norm of the solution  $h$  to the 2D SGN equation for initial data of the form (18) in dependence of time: on the left for the  $-$  sign in (18), on the right for the  $+$  sign.

For symmetry reasons the  $u_y$  solution is just the figure for  $u_x$  rotated by 90 degrees and therefore not shown.

## 6. LOCALIZED INITIAL DATA

In this section we study the time evolution of localized initial data. It is shown that initial data with radial symmetry develop into some annular structure with some depression near the center. It is argued that the solution near this center can be asymptotically characterized by a radially symmetric solution of the SGN equations. We did not find a stable structure with such initial data as a lump soliton for the KP I which provides support for the second part of the Main conjecture.

**6.1. Gaussian initial data.** As an example for localised initial data, we consider

$$(20) \quad h(x, y, 0) = \alpha \exp(-x^2 - y^2), \quad v_x = v_y = 0,$$

i.e., Gaussian initial data. Note that the code does not use the radial symmetry of the initial data.

For  $\alpha = 4$ , we use  $N_x = N_y = 2^{10}$  Fourier modes and  $L_x = L_y = 5$  with  $N_t = 10^3$  time steps for  $t \leq 5$ . Relative energy conservation is of the order of  $10^{-10}$ . The solution  $h$  for several times can be seen in Fig. 13. The initial hump evolves into some annular structure with radius increasing with time. Very similar figures can be obtained for  $\alpha = 2$  or  $\alpha = 8$ . The SGN equation appears to be defocusing in the sense that localised humps get dispersed.

Interestingly the initial hump turns into a depression wave in finite time, a wave with smaller elevation than the asymptotic value for  $h$ . To illustrate this better, we show in Fig. 14 on the left the solution  $h$  at the last shown time in Fig. 13 on the  $x$ -axis. It can be seen that the solution is getting close to the bottom of the basin. The infimum of the solution in dependence of time is shown on the right of

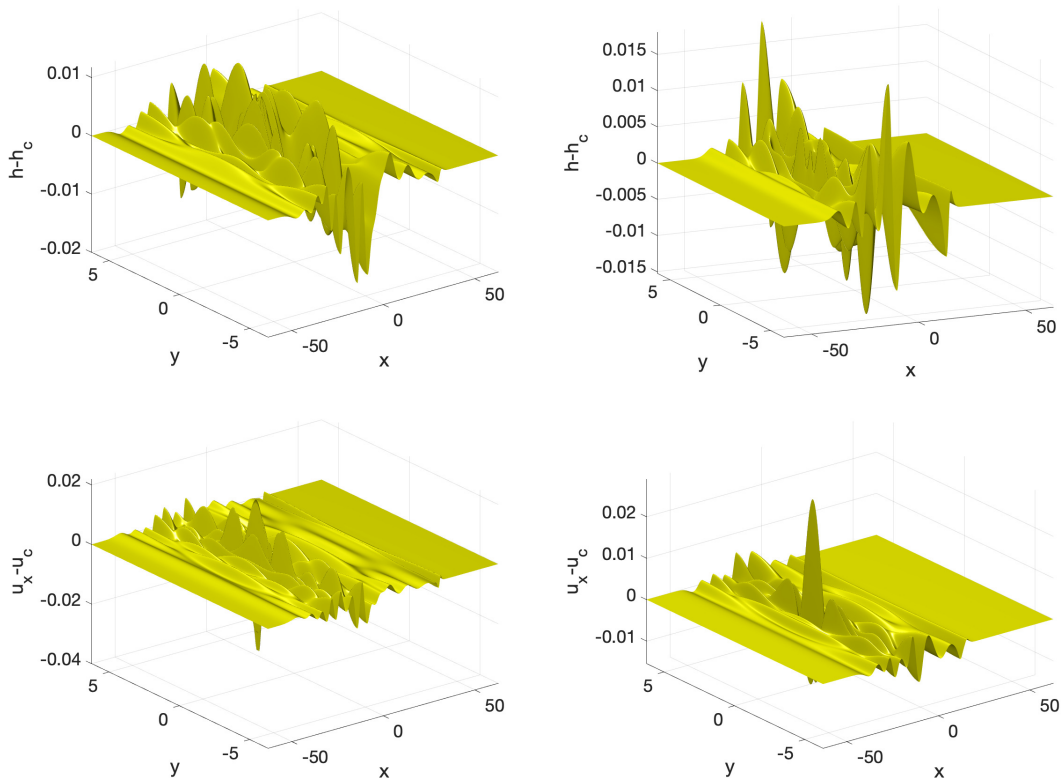


FIGURE 10. Difference of the solution to the 2D SGN equation for initial data of the form (18) and a fitted line solitary wave: on the left for the  $-$  sign in (18) for  $t = 30$ , on the right for the  $+$  sign for  $t = 20$ , the upper row for  $h$ , the lower for  $u_x$ .

the same figure. At  $t \sim 2.5$ , this infimum becomes smaller than  $h_\infty$  and continues to decrease. The no-cavitation condition appears to be always satisfied, and the DFT coefficients indicate that the solution stays smooth for all considered times.

The solution  $u_x$  to the SGN equation for the initial data (20) can be seen for several values of  $t$  in Fig. 15. The function  $u_y$  shows the same behavior rotated by 90 degrees for symmetry reasons and is not shown.

**6.2. Radially symmetric solutions.** The formation of a “cylinder-type” structure in the case of axisymmetric localized initial data suggests that the solution for long times becomes radially symmetric near the center of the annular structure: the position of the free surface is almost flat, no obvious oscillations can be seen. In the radially symmetric case, we can construct an exact solution to the SGN equations approximating this “flat” structure. More exactly, consider the SGN equations (1) in the polar coordinates ( $x = r \cos \phi$ ,  $y = r \sin \phi$ ). In the case where the azimuthal velocity  $u_\phi$  is zero and all other variables depend only on  $r$ , the

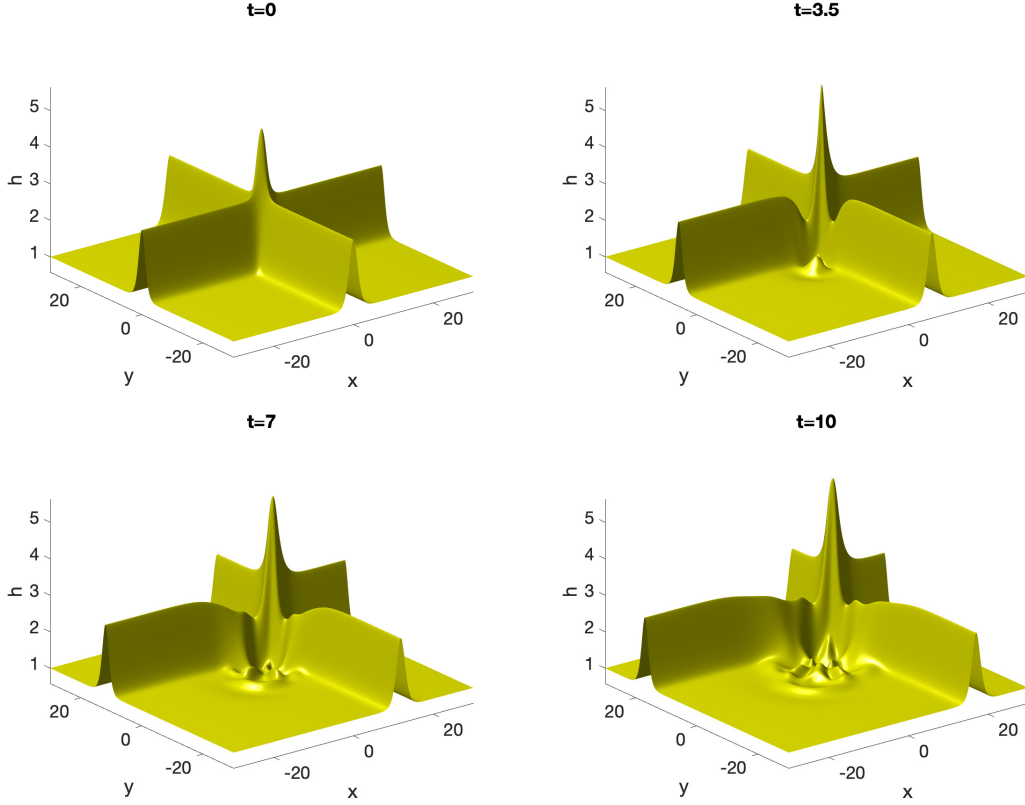


FIGURE 11. Solution  $h$  to the 2D SGN equation for initial data of the form (19) for several times.

governing equations for  $h$  and radial velocity  $u_r$  take a standard form:

$$\frac{\partial(rh)}{\partial t} + \frac{\partial(rhu_r)}{\partial r} = 0, \quad h \left( \frac{\partial u_r}{\partial t} + u_r \frac{\partial u_r}{\partial r} \right) + \frac{\partial p}{\partial r} = 0, \quad r = \sqrt{x^2 + y^2}$$

They admit the following exact solution

$$(21) \quad \tilde{h}(t) = \frac{h_0}{(c_0 + w_0 t)^2}, \quad \tilde{u}_r(t, r) = \frac{w_0 r}{c_0 + w_0 t},$$

with constants  $c_0$ ,  $h_0$  and  $w_0$ . We show the radial and azimuthal component of the velocity for  $t = 5$  for the situation shown in Fig. 15 in Fig. 16. It can be seen that the radial velocity shows almost the expected radial symmetry whereas the azimuthal component is of the order of  $10^{-7}$  (still much larger than the estimated numerical error) and almost vanishing near the origin.

We can fit the infimum of the solution  $h$  in Fig. 14 on the left to the asymptotic formula. This means we choose the parameters  $h_0/c_0^2$  and  $w_0/c_0$  such that  $h(1 + tw_0/c_0)^2$  is roughly constant. To this end we apply the algorithm [15] being distributed with Matlab as the command *fminsearch* for  $t \geq 3.75$  (the result



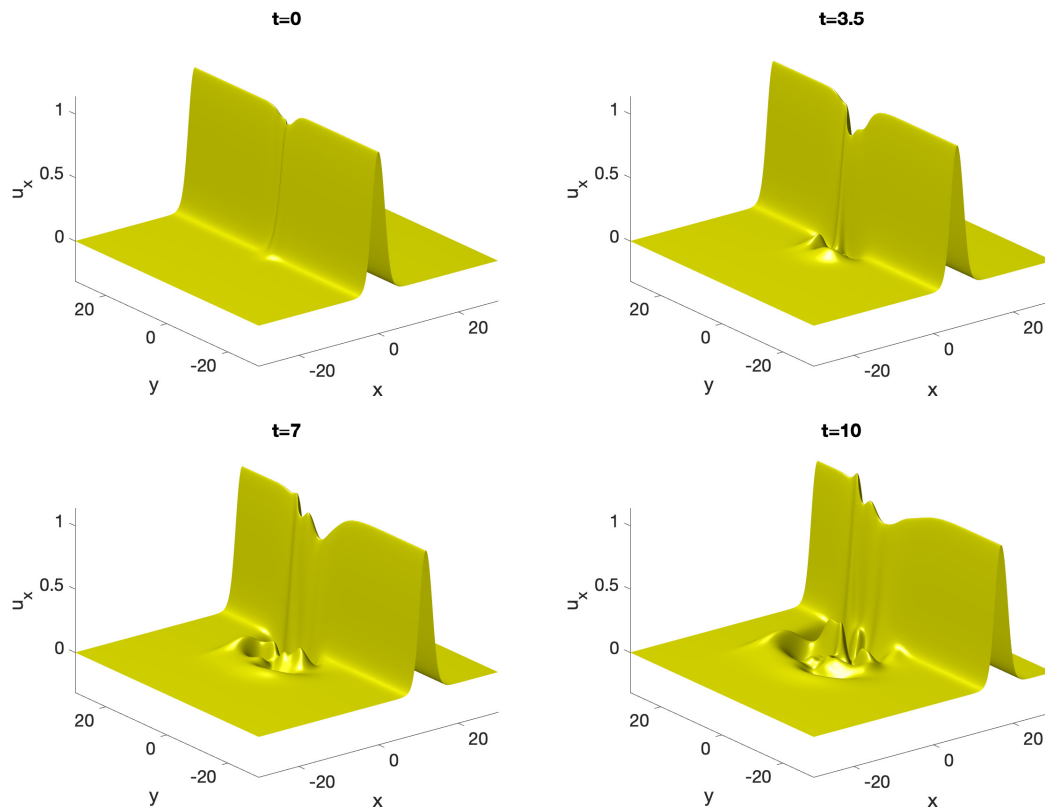


FIGURE 12. Solution  $u_x$  to the 2D SGN equation for initial data of the form (19) for several times.

does not change much if this time is slightly varied). We get  $h_0/c_0^2 = 0.1545$  and  $w_0/c_0 = -0.5117$ . The result of the fitting of the infimum of the solution can be seen on the left of Fig. 17. It can be seen that the fitting gives an excellent result (the residual on the fitted domain is of the order of  $10^{-3}$ ) which gives a strong indication that the solution near the origin follows the dynamics of the special solution (21). This is further confirmed by comparing the solution  $\tilde{u}_r$  with the fitted parameters to the radial component  $u_r$  of the velocity as shown on the right. The linear behavior in  $r$  can be clearly recognized.

## 7. CONCLUSION

In this paper we have presented a numerical approach to the 2D SGN equations based on a Fourier spectral method with the Krylov subspace technique GMRES to solve an elliptic equation. The code allowed to provide strong numerical evidence for the transverse stability of the line solitary waves of SGN as well as the defocusing character of the SGN equations in 2D. No stable structures localised in 2D were discovered. It was shown that radially symmetric initial data evolve into

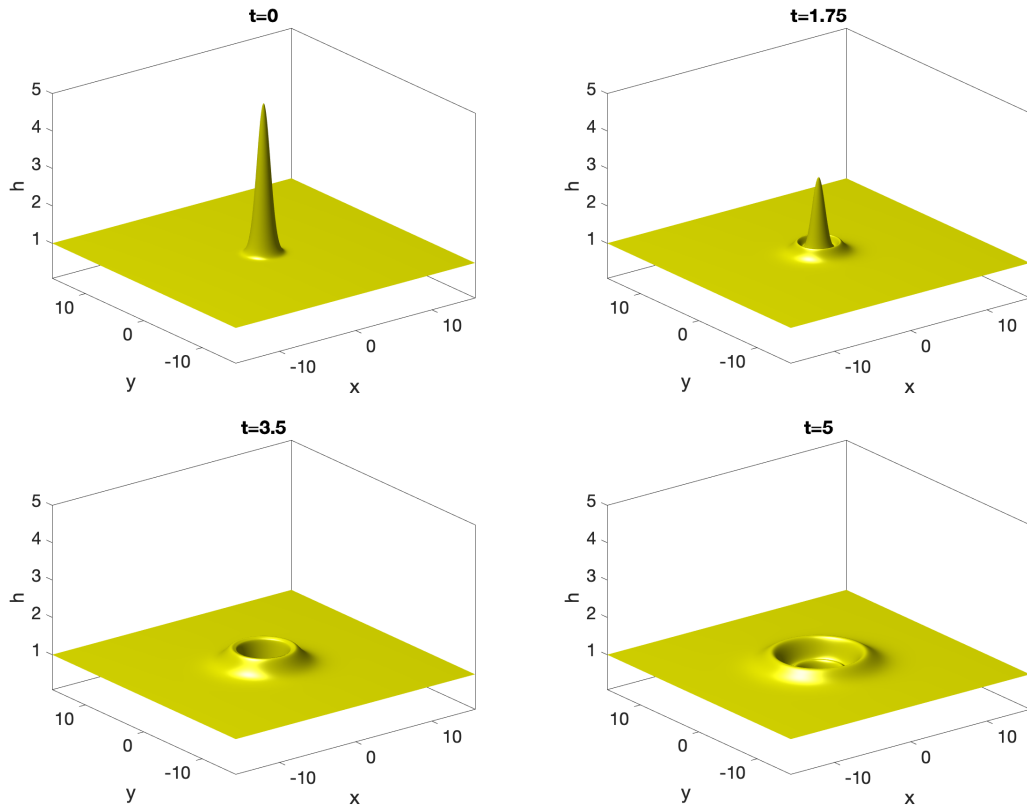


FIGURE 13. Solution  $h$  to the 2D SGN equation for initial data of the form (20) for several times.

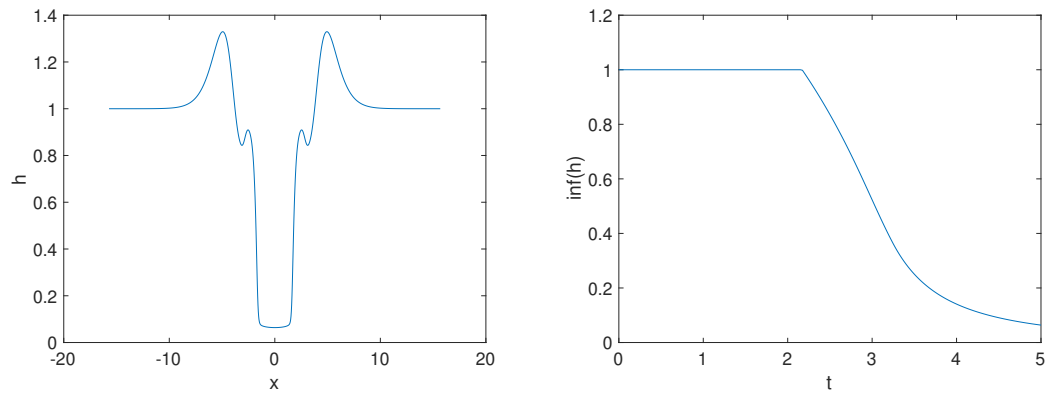


FIGURE 14. Solution  $h$  to the 2D SGN equation for initial data of the form (20) for  $t = 5$  on the  $x$ -axis on the left, and the infimum of the solution in dependence of time on the right.

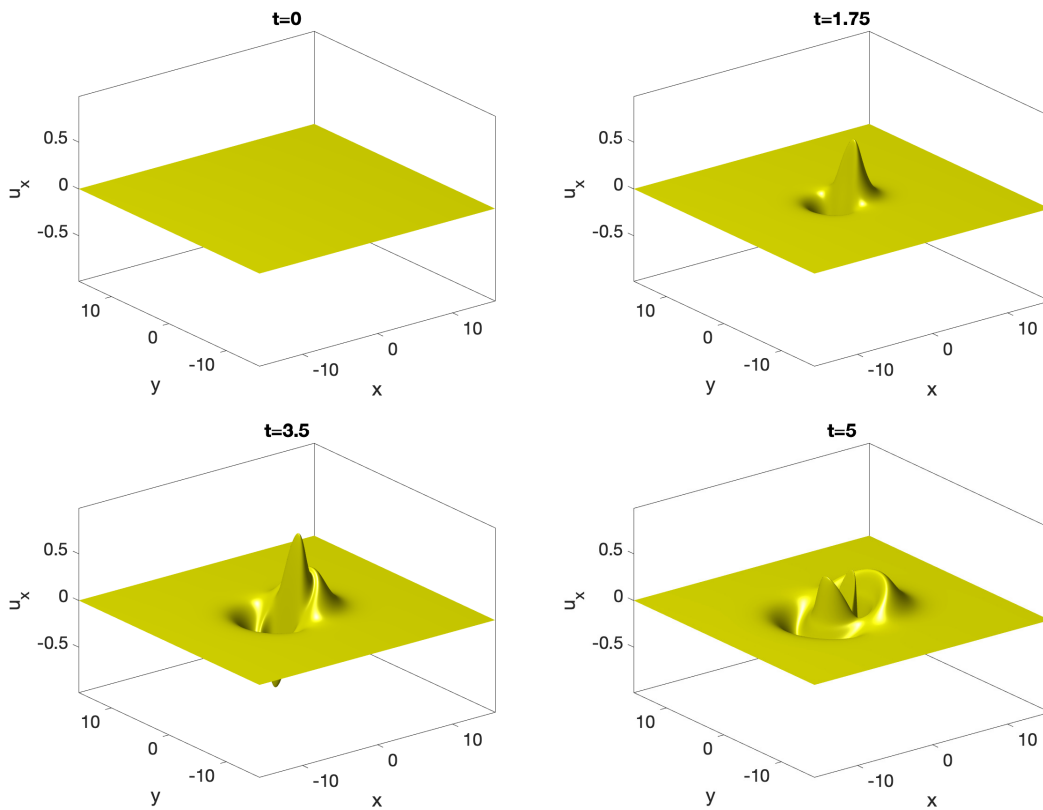


FIGURE 15. Solution  $u_x$  to the 2D SGN equation for initial data of the form (20) for several times.

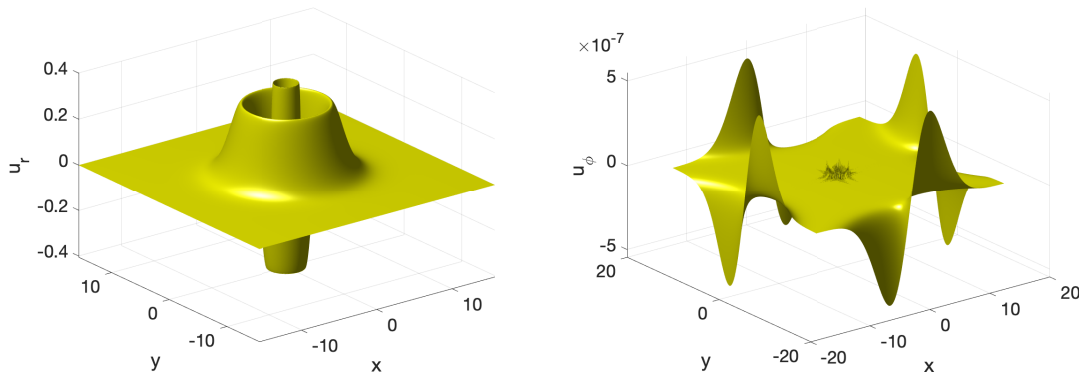


FIGURE 16. Velocity  $\bar{\mathbf{u}}$  for the 2D SGN equation for initial data of the form (20) for  $t = 5$ , on the left the radial component, on the right the azimuthal component.

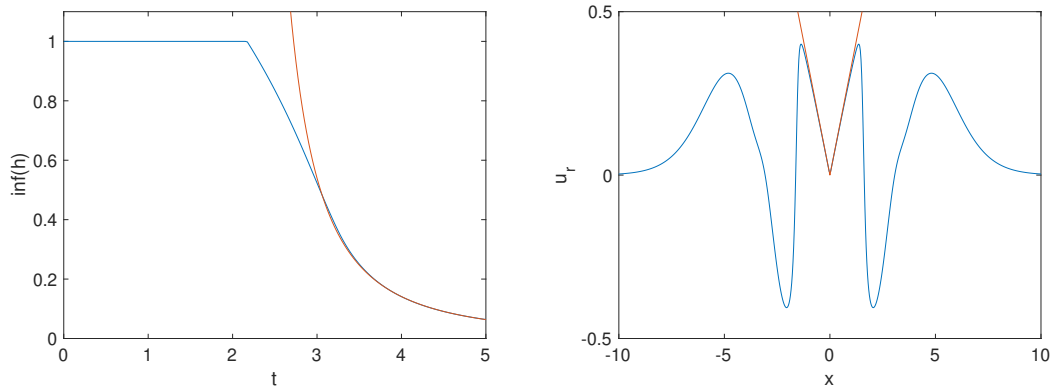


FIGURE 17. Infimum of the solution  $h$  to the 2D SGN equation for initial data of the form (20) with the fitted profile (21) in red on the left, and the radial component of the velocity in dependence of  $x$  with the fitted solution (21) in red on the right.

an annular structure with a depression near the center that can be asymptotically described via a special radially symmetric solution to the SGN equations. The no-cavitation condition appears to be satisfied at all times.

Stronger computers than the ones we had access for this paper (essentially a laptop) will be needed to address questions having been studied in 1D in [1]. An interesting such question will be the appearance of *dispersive shock waves* (DSW), zones of rapid modulated oscillations in the solutions. They appear in dispersive PDEs in the vicinity of shocks of the solutions to the corresponding dispersionless PDEs for the same initial data [3]. While 1D DSW for the SGN equations have already been actively investigated [2, 6, 18], their multi-dimensional analogues are still waiting to be studied.

Another interesting question is whether the SGN equation allows for shocks in finite time for smooth initial data. A comparison to the Camassa-Holm (CH) equation was presented in 1D in [1]. Since both CH and SGN are nonlocal and since it is known that CH solutions can have a blow-up (an explosion of some norm of the solution) for certain classes of initial data, a similar behaviour is possible for the SGN equations.

This will be the subject of further research.

## REFERENCES

- [1] V. Duchêne, C. Klein, Numerical study of the Serre-Green-Naghdi equations and a fully dispersive counterpart, *Discr. & Cont. Dyn. Syst. B*, 27(10), 5905-593 (2021) doi: 10.3934/dcdsb.2021300
- [2] G. A. El, R. H. J. Grimshaw and N. F. Smyth 2006 Unsteady undular bores in fully nonlinear shallow-water theory, *Phys. Fluids* **18** 027104.

- [3] G. A. El and M. A. Hoefer, Dispersive shock waves and modulation theory, *Physica D* **333**, 11-65 (2016)
- [4] S. Gavriluk, H. Kalisch & Z. Khorsand, A kinematic conservation law in free surface flow, *Nonlinearity*, **28** (2014) 1805–1821.
- [5] S. L. Gavriluk & V. M. Teshukov, Generalized vorticity for bubbly liquid and dispersive shallow water equations, *Continuum Mechanics and Thermodynamics*, **13** (2001) 365-382
- [6] S. Gavriluk, B. Nkonga, K.-M. Shyue & L. Truskinovsky, Stationary shock-like transition fronts in dispersive systems, *Nonlinearity*, **33** (2020), 5477-5509.
- [7] A. E. Green, N. Laws & P. M. Naghdi, On the theory of water waves, *Proc. R. Soc. Lond. A* **338** (1974), 43–55.
- [8] A. E. Green & P. M. Naghdi, A derivation of equations for wave propagation in water of variable depth, *J. Fluid Mech.* **78** (1976), 237–246.
- [9] C. Klein, Fourth order time-stepping for low dispersion Korteweg-de Vries and nonlinear Schrödinger equation, *ETNA Vol. 29* 116-135 (2008).
- [10] C. Klein and J.-C. Saut, Nonlinear dispersive equations — Inverse Scattering and PDE methods, *Applied Mathematical Sciences* 209 (Springer, 2022)
- [11] Y. Kodama, KP Solitons and the Grassmannians: Combinatorics and Geometry of Two-Dimensional Wave Patterns, *SpringerBriefs in Mathematical Physics* **22** (2017).
- [12] R. Krasny, A study of singularity formation in a vortex sheet by the point-vortex approximation, *J. Fluid Mech.* **167** (1986) 65–93.
- [13] D. Lannes, *The Water Waves Problem*, *Mathematical Surveys and Monographs*, vol. **188** (Amer. Math. Soc., Providence, 2013).
- [14] N. Makarenko, A second long-wave approximation in the Cauchy-Poisson problem, *Dynamics of Continuous Media*, v. 77 (1986), pp. 56-72 (in Russian).
- [15] J. C. Lagarias, J. A. Reeds, M. H. Wright, and P. E. Wright. Convergence Properties of the Nelder-Mead Simplex Method in Low Dimensions. *SIAM Journal of Optimization*. Vol. 9, Number 1, 1998, pp. 112-147.
- [16] O. Le Métayer, S. Gavriluk & S. Hank, A numerical scheme for the Green-Naghdi model, *J. Comp. Phys.* **229** (2010), 2034–2045.
- [17] Yi A. Li, Linear stability of solitary waves of the Green-Naghdi Equations, *Communications on Pure and Appl. Math.* **LIV** (2001), 501–536.
- [18] J. P. A. Pitt, C. Zoppou & S. G. Roberts, Behaviour of the Serre equations in the presence of steep gradients revisited, *Wave Motion* **76** (2018), 61–77
- [19] J. Miles & R. Salmon, Weakly dispersive nonlinear gravity waves, *J. Fluid Mechanics* **157** (1985), 519–531.
- [20] Y. Saad and M. H. Schultz. GMRES: a generalized minimal residual algorithm for solving nonsymmetric linear systems. *SIAM J. Sci. Statist. Comput.*, 7(3):856–869, 1986.
- [21] R. Salmon, *Lectures on Geophysical Fluid Dynamics*, Oxford University Press, 1998, ISBN 9780195355321.
- [22] F. Serre, Contribution à l'étude des écoulements permanents et variables dans les canaux, *La Houille Blanche* **8** (1953), 374–388.
- [23] C. H. Su & C. S. Gardner, Korteweg - de Vries Equation and Generalisations. III. Derivation of the Korteweg - de Vries Equation and Burgers Equation, *J. Math. Physics*, **10** (1969) 536–539.
- [24] S. Tkachenko, S. Gavriluk & J. Massoni, Extended Lagrangian approach for the numerical study of multidimensional dispersive waves: applications to the Serre-Green-Naghdi equations, *Journal of Computational Physics* (2023), 111901.
- [25] L. Trefethen. *Spectral Methods in Matlab*. SIAM, Philadelphia, PA, 2000.

AIX-MARSEILLE UNIVERSITÉ AND CNRS UMR 7343 IUSTI, 5 RUE ENRICO FERMI, 13453  
MARSEILLE, FRANCE, E-MAIL SERGEY.GAVRILYUK@UNIV-AMU.FR

INSTITUT DE MATHÉMATIQUES DE BOURGOGNE, UMR 5584, UNIVERSITÉ DE BOURGOGNE,  
9 AVENUE ALAIN SAVARY, 21078 DIJON CEDEX, FRANCE, INSTITUT UNIVERSITAIRE DE  
FRANCE, E-MAIL CHRISTIAN.KLEIN@U-BOURGOGNE.FR